Kennesaw State University

DigitalCommons@Kennesaw State University

Faculty Publications

11-23-2015

Calculation of Nonlinear Optical Damage from Space-time-tailored Pulses in Dielectrics

Thomas E. Lanier
Kennesaw State University, tlanier6@kennesaw.edu

Jeremy R. Gulley
Kennesaw State University, jgulley@kennesaw.edu

Follow this and additional works at: http://digitalcommons.kennesaw.edu/facpubs

Part of the Physics Commons

Calculation of nonlinear optical damage from space-time-tailored pulses in dielectrics

Thomas E. Lanier[a] and Jeremy R. Gulley[a]

[a]Department of Physics, Kennesaw State University, Kennesaw, GA, 30144, USA

ABSTRACT

Control of the time duration of a laser pulse as it focuses spatially in a material provides a means for delaying the onset of nonlinear effects during propagation. We investigate simultaneous space-time focusing (SSTF) of femtosecond radially-chirped annular pulses in Kerr dielectrics. The energy and temporal chirp of pulses incident upon a grating-grating-lens system are varied in simulations that solve the unidirectional pulse propagation equation. This system is modeled by inserting transformations that act on the electric field obtained from propagation from one component to the next. The propagation is coupled to the time evolution of the free charge density as a function of space. The resulting "ionization tracks" are taken as a metric for predicting material modification and/or damage in bulk fused silica. As expected from linear-optical considerations, the temporal pre-chirp determines the overall pulse duration as the focusing annulus closes. We find in addition that, for a given pulse energy, the temporal pre-chirp also determines the on-axis intensity distribution as energy collapses onto the propagation axis. This effect determines how the local ionization-induced decrease in refractive index shifts energy in time relative to energy arriving on-axis from the spatially collapsing beam. The magnitude of the pre-chirp can thus control the spatial structure of ionization that may lead to material modification and/or damage.

Keywords: ultrashort laser pulse, nonlinear propagation, ionization, pulse shaping, beam shaping, micromachining, material modification, bessel beam

1. INTRODUCTION

Optically-induced material modification and damage, often accompanied by laser filamentation, is commonly studied for the case of the ubiquitous Gaussian beam shape with a simple pulse shape in time, and simple spatial phase that corresponds to common focusing optics. Much work has been devoted to investigating material modification and damage in transparent dielectrics due to such waveforms with duration on the order of femtoseconds.[1–8] More recent studies have explored more exotic pulses that approximate Airy or Bessel spatial profiles, Airy time shapes, or some combination of these.[9–13] These waveforms have attracted interest because of their self-healing, accelerating, and/or non-diffracting properties. Bessel beams, in particular, have been studied in terms of their ability to extend filaments and/or material modification sites.[14–16]

Another departure from the standard Gaussian arises when pulses are spatially chirped. By angularly dispersing the frequency components of a broadband laser pulse (via diffraction gratings, for example), and recombining them gradually in space (using a lens, for example), the Fourier limits of spatial and temporal compression may be synchronized at a target (the focus of the lens, for example). This is called simultaneous space-time focusing (SSTF).[17, 18] It has been used to control and shorten the extent of a high-intensity focal region, thus controlling the extent and influence of nonlinear optical effects.[19–23] This control has led to various advances in laser writing and ablation applications.[24–26]

In this proceedings paper, we numerically explore material modification and damage due to radially chirped annular pulses via simulated propagation of time-chirped femtosecond pulses through the system shown in Fig. 1. The system imparts Bessel-like space-time attributes to an incident pulse engineered for cylindrically symmetric

---

SSTF in the bulk of fused silica. We first specify and briefly describe the spectral numerical propagation formalism used. Secondly, we describe the sequence of numerical transformations that corresponds to traversing the system, including a model for gratings consisting of a concentric array of circular grooves that is suited to the spectral propagation method. Next, we establish a basis for our study of annular SSTF in fused silica in terms of annular SSTF in vacuum, and then place a dispersive medium in the sample position. Finally, we present free carrier densities (termed "ionization tracks") as a function of space, which we regard as a predictor for plasma-induced material modification.

2. PROPAGATION FORMALISM

It is important to couple the material optical response to optical propagation described by a numerical method that captures the spatial as well as the temporal degrees of freedom accurately. In this section, we describe the theoretical background for our simulations of simultaneous space-time focusing of radially-chirped annular beams corresponding to the system shown in Fig. 1.
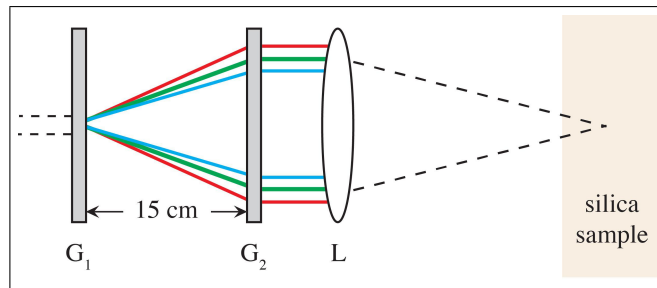

Figure 1. Schematic of the grating-grating-lens system for cylindrically symmetric SSTF. The two concentric gratings G_1 and G_2 have ring spacing $d = 10$ μm. The lens L has focal length $f = 200$ mm.

2.1 Spectral Propagation/Optical Nonlinearities

2.1.1 Unidirectional pulse propagation equation

Laser pulse propagation is computed in the retarded-time reference frame by numerically solving the unidirectional pulse propagation equation[27] under the assumption of cylindrical symmetry:

$$\partial_z E\left(k_\perp, \omega, z\right) = ik_z\, E\left(k_\perp, \omega, z\right) + \frac{i\,\omega^2}{2\epsilon_0 c^2 k_z}\, P^{\mathrm{NL}}(k_\perp, \omega, z) - \frac{\omega}{2\epsilon_0 c^2 k_z}\, J(k_\perp, \omega, z)\,. \tag{1}$$

Here, $k_z = \sqrt{k^2(\omega) - k_\perp^2}$ is the z-component of the wave vector with magnitude $k(\omega) = n(\omega)\,\omega/c$, ϵ_0 is the permittivity of free space, and the complex electric field array $E(k_\perp, \omega, z)$ is stored at discrete spatial frequencies and angular frequencies denoted here by $k_\perp$ and ω, respectively. The nonlinear source terms associated with P^{NL} and J are described in Section 2.1.3. This propagation scheme avoids making the paraxial approximation associated with many computational pulse propagation methods. In addition, it possesses the feature that linear propagation is exact within the limits of the accuracy of the linear refractive index $n(\omega)$ as derived from a Sellmeier equation. On the other hand, the method retains the unidirectional approximation and therefore not suited to optical situations involving large back reflections.[28] The evolution equation for spectral amplitudes A, related to E by $E(k_\perp, \omega, z) = \exp(ik_z z)A(k_\perp, \omega, z)$, is a set of ordinary differential equations, which we solve using a fourth-order Runge-Kutta library with adaptive stepping capabilities. See Appendix A for details.

Inverse spectral transforms take $E(k_\perp, \omega, z) \to E(r, t, z)$ to calculate the nonlinear source terms during each z step. The transformation $\omega \to t$ is done using a standard fast Fourier transform. In cylindrical coordinates the transformation $k_\perp \to r$ is accomplished via Hankel transform. This is performed by multiplication by the self-reciprocal matrix H_{ij} described in Section 2.1.2.

2.1.2 Hankel transform

The transformation $E(k_\perp, t) \xrightarrow{\text{HT}} E(r,t)$ is accomplished by the following discrete Hankel transform:[29–31]

$$E\,[\,r[i],t\,] = \sum_{j=1}^{N} H_{ij}\,E\,[\,k_\perp[j],t\,],\tag{2}$$

where

$$H_{ij} = \frac{2}{\alpha_{N+1}}\frac{J_0\,(\alpha_i\alpha_j/\alpha_{N+1})}{J_1^2\,(\alpha_j)},\tag{3}$$

J_1 denotes the Bessel function $J_1(x)$, and α_i is the ith zero of the Bessel function $J_0(x)$. Here, N is the number of radial coordinates $r[i] = (R_{\max}/\alpha_{N+1})\,\alpha_i$ and transverse wave vectors $k_\perp[i] = \alpha_i/R_{\max}$ to which the array $E\,[\,r[i],t[j]\,]$ is referenced. The inverse transform is accomplished by repeating the multiplication by H_{ij}.

It is worth noting that the matrix specified by Eq. 3 is suited to an algorithm that does not depend on its scaling. The transforms that preserve Parseval's theorem are:

$$f[i] = \frac{\alpha_{N+1}}{R_{\max}^2}\sum_{j=1}^{N} H_{ij}\,F_0[j] \qquad\qquad F_0[j] = \frac{R_{\max}^2}{\alpha_{N+1}}\sum_{i=1}^{N} H_{ji}\,f[i].\tag{4}$$

2.1.3 Nonlinear polarization and free current density

We calculate the nonlinear polarization at a particular position (r- and z-dependence suppressed) as

$$P^{\text{NL}}(t) = 2n_0\epsilon_0 n_2\left[\int_{-\infty}^{t} R(t-\tau)I(\tau)d\tau\right]E(t),\tag{5}$$

where $I = \frac{1}{2}n_0\epsilon_0 c\,|E|^2$, n_0 is the refractive index at the pulse center frequency ω_0, n_2 is the nonlinear refractive index, and $R(t)$ is the Raman response function.[28] The free current density J is calculated at each r by integrating the following coupled equations during each z step as described in Ref. 28:

$$\frac{dJ}{dt} + \frac{J}{\tau_{\text{c}}} = \frac{q^2}{m}\rho E\tag{6}$$

$$\frac{d\rho}{dt} = W_{\text{PI}}(|E|)\left(1 - \frac{\rho}{\rho_n}\right) + W_{\text{aval}}(I)\rho\tag{7}$$

Here, ρ is the density of free carriers, $W_{\text{aval}} = \sigma I/E_{\text{g}}$ is the ionization rate associated with avalanching, $\sigma = q^2/(\epsilon_0 n_0 mc) \times \tau_{\text{c}}/(1+\omega_0^2\tau_{\text{c}}^2)$ is the cross section for inverse bremsstrahlung, W_{PI} is the photoionization rate calculated from the Keldysh model[32] as in Ref. 6, and all other parameters are defined in Table 1.

2.2 The Incident Pulse Field

A spatially chirped optical pulse may be focused such that the distribution of optical energy in space and time evolves toward one that is maximally compressed in both dimensions simultaneously, even in vacuum. This occurs because the band-limited, shortest-duration pulse is gradually Fourier-synthesized by virtue of the space-time overlap of the pulse frequency content as it approaches the focus. In the linear optical regime of bulk fused silica, this remains true as long as dispersion of the pulse spectrum is considered in the design of the initial pulse. In this section, we describe the construction of the pulse incident upon the sample surface. In our simulations, propagation between optical elements is assumed to be linear and is therefore accomplished by multiplying $E(k_\perp,\omega,z)$ by the linear propagator $\exp(ik_z\Delta z)$. We emphasize here that k_z is a function of $k_\perp$ and ω. The optical components of the system shown in Fig. 1 are modeled by r- and ω-dependent transformations that act on $E(r,\omega)$. Propagation through the system to the sample surface thus amounts to a sequence of ~ 7 non-commuting transformations that act on the pulse field array*. This versatile simulation scheme maintains an intuitive correspondence with experiment, is capable of capturing subtle/realistic linear-optical effects that modify the pulse en route to the sample surface, and accommodates a wide variety of input pulses. The transformations by which we model the optical components are described in the following sections.

---

*It is worth noting that propagation between optical elements is not subject to the usual computational constraints typically imposed by upper limits on step size.

Table 1. Parameters used in simulations.

Symbol	Description	Value	Unit
n_0	Linear index of refraction	1.453	
n_2	Nonlinear index of refraction	3.00×10^{-20}	$\mathrm{m^2/W}$
E_g	Band gap energy	9.00	eV
m	Reduced electron-hole mass	7.834×10^{-31}	kg
τ_c	Free electron collision time	1.00×10^{-15}	s
ρ_n	Maximum plasma density	2.20×10^{28}	$\mathrm{m^{-3}}$
q	Elementary charge	1.602×10^{-19}	C
ϵ_0	Vacuum permittivity	8.854×10^{-12}	F/m
c	Speed of light	2.998×10^8	m/s

2.2.1 Pre-chirp

It is common to work with initially time-chirped pulses in SSTF systems because of the frequency dependence of the optical path through such systems. Computationally speaking, the input pulse to the optical system shown in Fig. 1 may be chirped in time by transforming the electric field as

$$E(r, \omega) \rightarrow \exp(ib_2(\omega - \omega_0)^2)\, E(r, \omega), \tag{8}$$

where b_2 parameterizes the extent and sign of the chirp. For the 800 nm, 40 fs pulses we consider, b_2 is positive and on the order of 10^{-27} s^2. Multiplication by the quadratic spectral phase stretches the pulse in time without modifying its spectral width, and corresponds to the action of a standard pulse-stretching device (or detuning of the compressor stage of a common chirped-pulse amplification system). This attribute of the input pulse will be referred to as the "pre-chirp". It will allow for variable compensation of the frequency dependence of the optical path length between gratings (see Fig. 1).

2.2.2 Grating transformations

A particular diffraction order exiting a grating may be constructed mathematically from the pulse incident upon the grating by shifting its spatial frequencies in accordance with the properties of the grating.[33] For the circular gratings and cylindrical coordinates considered here, we employ a generalized Hankel shift,[34, 35] thus producing the mth conical diffraction order:

$$E(k_\perp, \omega) \rightarrow \int_0^\infty E(r, \omega)\, J_0(r\Delta k)\, J_0(k_\perp r)\, r\, dr \tag{9}$$

$$= \mathrm{HT}\left[\, E(r, \omega)\, J_0(r\Delta k)\, \right].$$

where HT denotes the Hankel transform, and

$$\Delta k = \Delta k(\omega) = \frac{2\pi m}{d}\left(2 - \frac{\omega}{\omega_0}\right) \tag{10}$$

describes the diffraction of the circular grating with ring spacing d. Equation 10 follows from carrying out a procedure analogous to that in Refs. 33 and 36. Simply put, Eq. 10 is used to model a circular grating by transforming the pulse field as

$$E(r, \omega) \rightarrow J_0(r\Delta k)\, E(r, \omega), \tag{11}$$

which is owing to Eq. 9 and the fact that the Hankel transform is self-reciprocating.[37]

Taking $E(r, \omega) = A(r) S(\omega)$ to be the input pulse, Gaussian in time with arbitrary pre-chirp (see Section 2.2.1), and with beam shape given by an apodizing function $A(r)$, the $k_\perp$-shifted frequency superposition has the form of an apodized Bessel beam:[38,39]

$$E'(r, t) = \int_{-\infty}^{\infty} S(\omega) A(r) J_0(r \Delta k) e^{-i\omega t} d\omega \tag{12}$$

Thus, after G_1, the pulse field is an apodized frequency superposition of Bessel beams with axicon angles varying with frequency ω according to Eq. 10. We choose a Gaussian apodizing function $A(r) = \exp\left(-r^2/w^2\right)$, which corresponds to taking the spatial beam profile of the input pulse to be a collimated Gaussian with $1/e^2$ intensity width w. The results presented in this paper use $w = 2$ mm, and $m = 1$, and $d = 10$ μm in Eq. 10. Two examples are shown in Fig. 2.
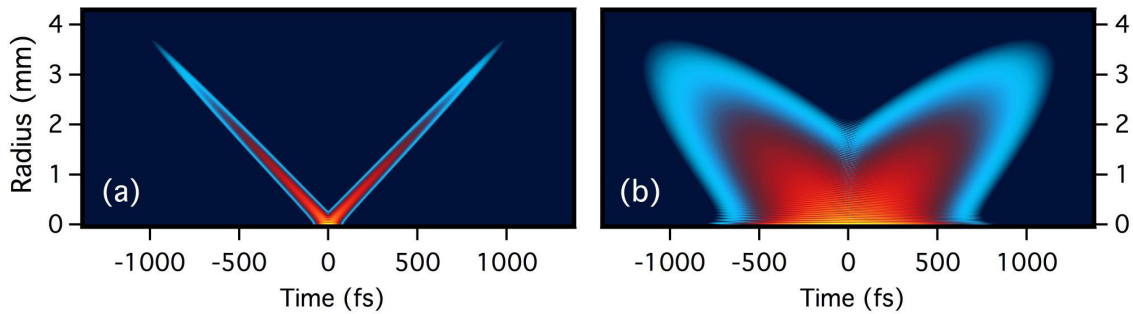

Figure 2. Logarithmic intensities after the first circular grating G_1 for two different choices of pre-chirp. The color map extends down 6 orders of magnitude below the peak in each case. (a) The case $b_2 = 0$ ($\tau_0 = 40$ fs). (b) The case $b_2 = 2618$ fs^2 ($\tau_0 = 365$ fs).

At G_2, the transformation is repeated. This time, however, a pair of $m = 1$ conical diffraction orders is produced. One of these diffracts into a larger cone angle while the other is conjugated by the second $d = 10$ μm grating G_2. The former is filtered from $E(k_\perp, \omega)$ by zeroing the electric field in the relevant region in $(k_\perp, \omega)$-space. The latter is the collimated, radially chirped annulus (RCA) that is propagated toward the lens (refer to Fig. 1). This filtering corresponds to physically blocking the outer non-collimated diffraction order.

Up to this point, the grating transformation described above fails to account for losses, which may depend on frequency/exit angle (blaze). While this could be introduced given a blaze function $B(k_\perp)$ to be multiplied by $E(k_\perp, \omega)$, we use $B(k_\perp) = 1$ and set the pulse energy before entering the sample by appropriately scaling the field. These conventions correspond to a grating blaze that diffracts the 800 nm, 40 fs pulse uniformly, and to a pulse energy measurement somewhere between the lens and sample.

2.2.3 Lens transformation

The action of a lens is modeled by the following transformation:

$$E(r, \omega) \rightarrow \exp\left(i\frac{\omega}{c}\left[n(\omega)L(r) + (d_0 - L(r))\right]\right) E(r, \omega), \tag{13}$$

where the lens thickness function $L(r) = d_0 - \frac{r^2}{2}\left(R_1^{-1} - R_2^{-1}\right)$ corresponds to the thin lens approximation.[33] Here, d_0 is the lens center thickness, $n(\omega)$ is the frequency dependent refractive index of the lens material as described by a Sellmeier equation, R_i are the radii of curvature, and the surrounding medium is treated as vacuum. Quite independent of its use as the sample in this paper, we choose fused silica as the lens material. A biconvex singlet lens of nominal focal length f is obtained by setting $R_1 = -R_2 = 2f(n_0 - 1)$, where n_0 is the lens refractive index at the pulse center frequency. In Eq. 13, the phase quadratic in r and roughly linear in ω produces the curved phase and pulse fronts that result from propagation through a lens. Spatially dependent group velocity dispersion and chromaticity of the lens are thus accounted for to infinite dispersion order.

We note that, as a practical consideration, a compensating phase $\exp\left(-i\frac{\omega}{v_g}L(r_0)\right)$, is also applied to shift the entire waveform in time, keeping it centered in the retarded time frame window. Here, r_0 is approximately equal to the radial position of the spatial component to be kept centered, and $v_g = \left(\frac{dk}{d\omega}\big|_{\omega_0}\right)^{-1}$ is the group velocity in the lens material derived from $n(\omega)$. For a more standard beam with intensity distribution concentrated on-axis, r_0 would be taken to be 0, but this is not the case for an annular spatial distribution.

3. NUMERICAL SIMULATIONS

We now discuss the numerical propagation of the pulses described in the Section 2.2. As a preliminary, we describe the optics in vacuum, and then show how the dynamics are modified by the insertion of a dielectric material in the sample position.

3.1 SSTF in Vacuum

SSTF of a broadband pulse occurs provided its frequencies are properly arranged in space and time. Figure 3 shows the effect occurring in vacuum, where two 1-μJ pulse intensities are plotted for various z-positions between the lens and its geometric focus. Figure 3 (a) shows the tilt of pulse spectrum versus radius for the pulse at the z-position of the lens. Figure 3 (b) shows the initially unchirped 40 fs pulse as it focuses after passing through the system shown in Fig. 1. Fig. 3 (c) shows the case $b_2 = 2618$ fs^2, in which the pulse has been positively chirped to $\tau_0 = 365$ fs prior to the first grating. As a result, the different inter-grating optical paths taken by the pulse's frequency components are compensated, and a near-bandwidth-limited 43.7 fs pulse is gradually Fourier-synthesized as it approaches the focus. Most importantly, the z-gradient of the optical power density is increased significantly relative to ordinary spatial focusing. We emphasize that material dispersion in the propagation medium is not at play here: SSTF occurs in vacuum given an appropriately tuned pre-chirp.
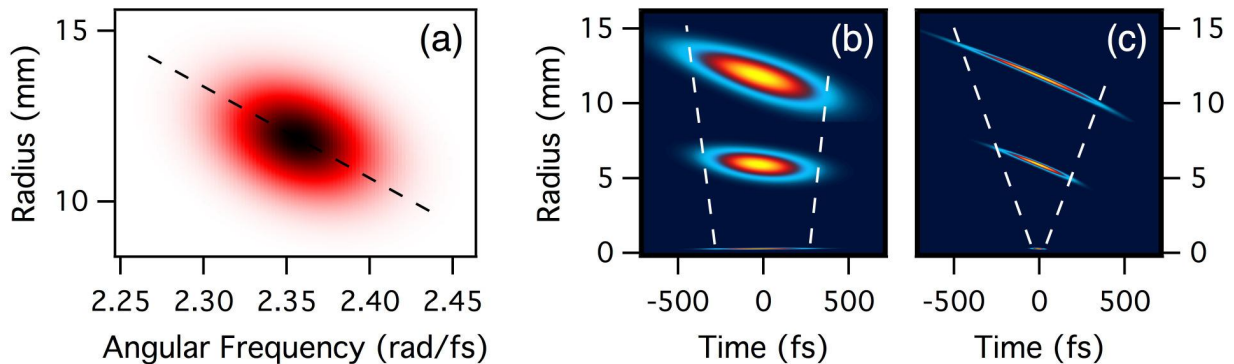

Figure 3. Simultaneous space-time focusing in vacuum of 1-μJ radially chirped annular pulses. (a) Tilted $r\omega$-spectrum just after G_2. (b)-(c) Normalized intensities for various propagation distances (superposed). In each case, propagation distances as measured from the $f = 200$ mm lens are 0 mm (top), 100 mm (middle), and 195 mm (bottom). (b) The initially bandwidth-limited 40 fs pulse. Peak intensities (TW/m^2) are 0.014 (top), 0.055 (middle), and 25.0 (bottom). (c) The positively pre-chirped 365 fs pulse. Peak intensities (TW/m^2) are 0.11 (top), 0.45 (middle), and 190 (bottom). Dashed lines are a guide for the eye.

3.2 SSTF in Dispersive Media

If a dispersive sample is positioned in the beam for bulk material modification, optimal time-focusing requires that material dispersion be compensated by adjusting the pre-chirp. Considering for the moment only linear optics, the frequency-dependent optical path lengths previously discussed in terms of the geometry of Fig. 1 are now subject to the additional effects of variable refraction and phase velocity across the spatial components of the radially chirped, focusing waveform. Furthermore, nonlinear optical processes play an increasing role in the

propagation as the pulse annulus closes on itself and compresses in space and time. These observations highlight the value of a fully spectral propagation scheme that captures linear dispersion trivially[†] while accommodating nonlinear source terms that are customizable to a given physical setting.

Better understanding of nonlinear propagation of the RCA through its nonlinear focus in the fused silica sample is facilitated by comparison with the case of a Gaussian beam (denoted hereafter as GB) of the same numerical aperture (NA ~ 0.06). Figure 4 shows example cases before reaching and during the nonlinear focus. Here, the pulse energy has been set to 0.7-μJ before entering the sample. For the GB case, panes (a) and (b) of
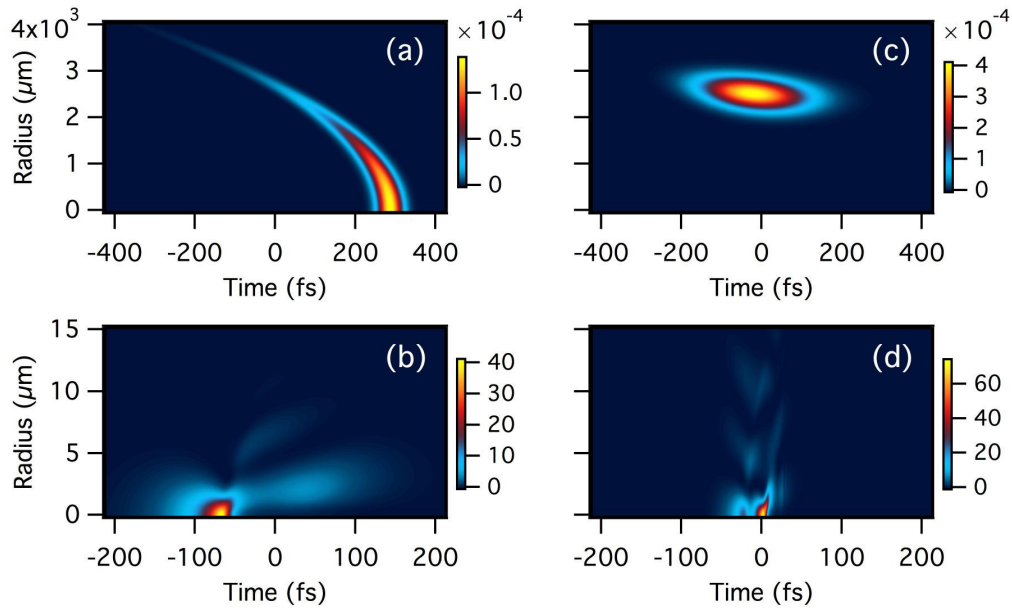

Figure 4. Intensities (TW/cm^2) of 0.7-μJ pulses before and during the nonlinear focus for cases (a)-(b) GB and (c)-(d) RCA with $b_2 = 1100$ fs^2 ($\tau_0 = 158$ fs). Sample depths are (a) 10 mm, (b) 72.65 mm, (c) 10 mm, (d) 72.15 mm.

Fig. 4 show the onset of pulse splitting that occurs in the focal region as plasma is generated and filamentation occurs.[40,41] Plasma-induced refractive index decrease arrests the spatial collapse due to Kerr self-focusing, and energy in the early-time pulse wing is temporally advanced. At the same z-position, energy in the late-time pulse wing partially diffracts away from the propagation axis, but subsequently re-focuses to the axis due to Kerr refractive index increase. Eventually, the time front of the pulse partially shears apart from its temporal rear. In this way, the quasi-stable balance of these nonlinear effects, along with ordinary beam diffraction, establishes an intensity distribution with multiple maxima in time.

Panes (c) and (d) of Fig. 4 show the analogous development of the RCA intensity. As the RCA pulse approaches the focus, its "ring thickness", and because of SSTF its time width, decrease as the ring closes onto the propagation axis. In other words, the distribution in Fig. 4 (c) becomes narrower in both r and t dimensions as energy converges on $r = 0$. At $z = 72.15$ mm (pane (d)), the Kerr nonlinearity is distorting the outer rings of the Bessel-like distribution and its central maximum, where plasma generation is most prominent. The process of filamentation thus develops as a complex interplay between plasma-induced time-advance of on-axis energy, Kerr collapse and re-focusing, Kerr-induced time-delay of energy, and continued deposition of additional energy to the propagation axis as the waveform advances in z.

In the next section, we shift our attention to the ionization tracks left by these pulses, which are regarded as a metric for material modification and damage.

_____

[†]In other words, at essentially no computational cost.

4. RESULTS: IONIZATION IN THE BULK

The maximum free carrier densities $\rho_{\max}(r, z)$ reached during the pulse time window have been regarded as a predictor in the context of laser damage and material modification studies.[6,42] Our calculations of these ionization tracks are presented in this section.

Figure 5 shows the ionization tracks from RCA pulses with various pre-chirp and energy, with GB results for comparison. In this figure, columns correspond to the sequence of pulse energies: 0.9 μJ, 0.7 μJ, 0.5 μJ. Rows correspond to the sequence of pre-chirps: $b_2 = 2000$ fs^2 ($\tau_0 = 280$ fs), $b_2 = 1700$ fs^2 ($\tau_0 = 239$ fs), $b_2 = 1100$ fs^2 ($\tau_0 = 158$ fs), and $b_2 = 900$ fs^2 ($\tau_0 = 131$ fs). Row 5 contains results from the GB with $\tau_0 = 40$ fs. Each color map applies to its respective column, and is set by the peak density occurring in Row 3.
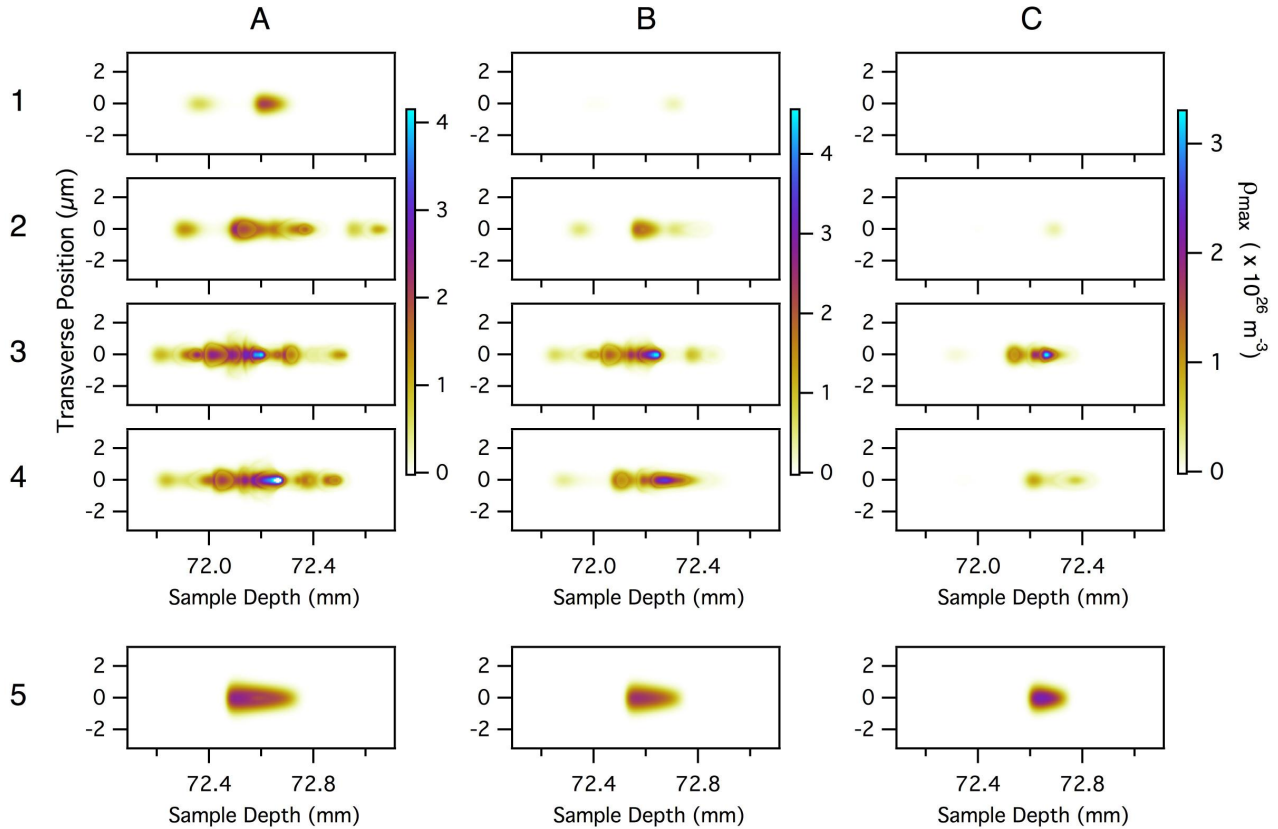

Figure 5. Ionization tracks $\rho_{\max}(r, z)$ from pulses with various pre-chirp and energy. Pulse energy varies by column. Pre-chirp varies by row. Row 1: RCA with $b_2 = 2000$ fs^2 ($\tau_0 = 280$ fs). Row 2: RCA with $b_2 = 1700$ fs^2 ($\tau_0 = 239$ fs). Row 3: RCA with $b_2 = 1100$ fs^2 ($\tau_0 = 158$ fs). Row 4: RCA with $b_2 = 900$ fs^2 ($\tau_0 = 131$ fs). Row 5: GB with $\tau_0 = 40$ fs. Columns correspond to pulse energies: A: 0.9 μJ, B: 0.7 μJ, C: 0.5 μJ. Each color map is set by the peak of the data shown in Row 3. Note that the color map of case 4A is saturated on-axis at $z \sim 72.25$ mm (displayed in white), where $\rho_{\max}$ reaches 4.61×10^{26} m^{-3}.

The pre-chirp parameter has a significant impact on the morphology of ionization tracks, and also affects the peak density reached. The overall trend identifiable in Fig. 5 indicates that pulse energy and pre-chirp may be tuned to produce a result with peak structure that is highly localized (see entry 3C) as compared with ordinary Gaussian beam/pulse focusing. In other words, from a laser materials processing standpoint, more precise targeting in the bulk may be achieved. We note that this pre-chirp value ($b_2 = 1100$ fs^2, $\tau_0 = 158$ fs) was derived from simulations performed with nonlinear source terms excluded (switched off) for the purpose of

determining the value that results in optimal SSTF according to linear optics[‡]. It is possible that finer tuning of this parameter (as well as energy, for that matter) may produce a better-localized ionization track.

On the other hand, this general trend in parameter space does not complete the story. While the pre-chirp corresponding to Row 3 at first glance produces the strongest ionization for a given energy, the result in entry 4A saturates the color map[§], which is set by the data in entry 3A. This indicates a nontrivial relationship between ρ_{max} and the pulse energy/pre-chirp parameter space. This of course arises from the complex interplay of nonlinearities as discussed in Section 3.2.

5. DISCUSSION

This proceedings paper has investigated laser pulse filamentation and damage by pulses whose duration is short during the influence of free carriers, and whose spectrum is single-peaked[¶]. We include a standard third-order Kerr nonlinearity, and the influence of multiphoton, tunneling, and avalanche ionization. While the Keldysh theory is not designed for the complex waveforms we investigate, it is commonly applied to pulsed propagation, parameterized by the pulse center frequency and instantaneous intensity. In addition, the model for avalanche ionization lacks a full non-equilibrium treatment via coupling with a Boltzmann transport equation. The associated simplifications have become commonplace in propagation simulations, at least in the context of high-dimensional ones capable of describing the spatial effects so crucial to phenomena like filamentation. The approach may be expected to fail when dynamical avalanche dominates, or in the case of mixed-color pulses. Since the pulses we investigate have short durations during those stretches of propagation which are impacted by ionization, and are constructed from the output of common femtosecond laser sources by linear means, we feel that adhering to this paradigm for the coupling of material response with nonlinear beam/pulse propagation is acceptable in this context.

Taking the free carrier densities $\rho_{max}(r,z)$ as a measure, the RCA cases come to a nonlinear focus earlier than the GB (note the shifted abscissas in Fig. 5). We attribute this shift to the way numerical apertures were equated: We define the numerical aperture of the RCA as r_0/f, where $r_0 = 11.83$ mm is the radial position of the peak intensity of the RCA after the lens transformation. The NA ~ 0.06 GB was then constructed according to standard expressions for Gaussian beams. The correspondence between these numerical apertures may be expected to be imperfect. It is to this ambiguity that we attribute the shifted nonlinear focus depths.

We note that the NA used in this paper was chosen as a compromise between computational size constraints and the higher-NA focusing conditions common to laser machining. Similarly, the amount of radial chirp is limited by our choice of annulus size, and could be increased in experiments. SSTF is a fundamental wave propagation phenomenon that does not rely on special effects due to material properties, linear or nonlinear. For this reason, we expect that the general features of our results may be extrapolated to larger radial chirps and the larger numerical apertures that are common in the context of laser materials processing.

Finally, we point out that these simulations model a single laser pulse, i.e, a laser running in single-shot mode. It is possible that features of our results like the better-localized peak structure in $\rho_{max}(r,z)$ (see Fig. 5 entry 3C) may be compounded by a laser source operating in its natural state - i.e, at a repetition rate of perhaps 1 kHz.

6. CONCLUSION

We present a model for the transformation of the output of common laser sources by a system of circular gratings and a lens, and numerically propagate the resulting space-time-focusing field in fused silica glass. These simulations reveal the influence of nonlinear optical effects on the focusing of these unconventional pulses, and suggest novel approaches to laser machining of solids. In particular, ionization tracks in the bulk show more localized (sub-micron) ionization peaks when compared to those of a Gaussian pulse of the same energy and numerical aperture.

[‡]In other words, to provide a reference for subsequent simulations with nonlinearities switched on.
[§]The density reaches a peak of 4.61×10^{26} m^{-3}.
[¶]In other words, we have not combined pulses of different colors - a more difficult situation to model.

APPENDIX A. SIMULATION DETAILS

A.1 Spatial Resolution Adjustment

The vastly different spatial scales of the field at the lens and the field at the nonlinear focus demand a robust tool for increasing the r-space grid resolution and, separately, decreasing N as the field propagates toward the focal region. This is owing to the initially large demands on the grid resolution and extent in $k_\perp$-space associated with the chosen focusing conditions and annular beam shape, and the increasing computational requirement per space point as the beams enter the focal region. We increase the r-space grid resolution by first interpolating the unevenly-spaced $k_\perp$-dependence of the magnitude and phase of E to an evenly-spaced set that includes the origin. The field at the origin is extrapolated from the interpolation function. Then, we downsample by two fold and zero-pad the result to effect the so-called exact interpolation in r-space. Finally, we interpolate back to a Hankel transform $k_\perp$ array with twice the original extent. This reduces the resolution in $k_\perp$-space by a factor of 0.5, but as the distance from the r-coordinate origin of the converging beam decreases, the requirements on the grid that resolves the phase in $k_\perp$-space are correspondingly relaxed.

We decrease N similarly, but with the $k_\perp$-space downsampling replaced by cropping some permissible portion of outer points in r-space. Inverse procedures are performed as necessary/permissible, for example, after energy leaves the nonlinear focus and diverges spatially. The z-positions at which all of these coordinate rescalings are performed were selected manually, on a case-by-case basis.

A.2 Adaptive Stepping

Because the system involves a pulse that evolves from one with negligible nonlinearity to a highly nonlinear focus, the numerical propagation lends itself to an adaptive stepping algorithm. The simulations performed in this study comprised a mixed approach, where constant step size run segments were designed with the help of adaptively stepped preliminary run segments, as well as convergence tests of the adaptive stepper.

A.3 Ionization Calculation

The calculations related to ionization come at significant computational expense per radial coordinate. Also, plasma generation is an extremely nonlinear process, being very much negligible for most of the field strengths occurring in the UPPE computational domain. These features mean that it is unnecessary to perform the plasma calculation for all z-positions during the approach to the nonlinear focus, and for all stored radial coordinates. In practice, we switch on the plasma contribution to the material response at a z-position where the pulse peak intensity reaches 10^{15} W/m^2, and confine the calculation to radial coordinates with a peak electric field of 10^7 N/C or greater, regardless of z-position.

A.4 Nonlinear Polarization

The nonlinear polarization given in Eq. 5 is included for all z-positions within the sample, and for all radial coordinates, regardless of z-position.

REFERENCES

[1] Wu, Z., Jiang, H., Sun, Q., Yang, H., and Gong, Q., "Filamentation and temporal reshaping of a femtosecond pulse in fused silica," *Phys. Rev. A* **68**, 063820 (2003).

[2] Nguyen, N., Saliminia, A., Chin, S., and Vallée, R., "Control of femtosecond laser written waveguides in silica glass," *Appl. Phys. B* **85**(1), 145–148 (2006).

[3] Mishchik, K., D'Amico, C., Velpula, P. K., Mauclair, C., Boukenter, A., Ouerdane, Y., and Stoian, R., "Ultrafast laser induced electronic and structural modifications in bulk fused silica," *J. Appl. Phys.* **114**(13) (2013).

[4] Sun, Q., Asahi, H., Nishijima, Y., Murazawa, N., Ueno, K., and Misawa, H., "Pulse duration dependent nonlinear propagation of a focused femtosecond laser pulse in fused silica," *Opt. Express* **18**, 24495–24503 (2010).

[5] Onda, S., Watanabe, W., Yamada, K., Itoh, K., and Nishii, J., "Study of filamentary damage in synthesized silica induced by chirped femtosecond laser pulses," *J. Opt. Soc. Am. B* **22**, 2437–2443 (2005).

[6] Couairon, A., Sudrie, L., Franco, M., Prade, B., and Mysyrowicz, A., "Filamentation and damage in fused silica induced by tightly focused femtosecond laser pulses," *Phys. Rev. B* **71**, 125435 (2005).

[7] Guo, H., Jiang, H., Fang, Y., Peng, C., Yang, H., Li, Y., and Gong, Q., "The pulse duration dependence of femtosecond laser induced refractive index modulation in fused silica," *J. Opt. A Pure Appl. Op.* **6**(8), 787 (2004).

[8] Herbstman, J. F. and Hunt, A. J., "High-aspect ratio nanochannel formation by single femtosecond laser pulses," *Opt. Express* **18**, 16840–16848 (2010).

[9] Polynkin, P., Kolesik, M., Moloney, J. V., Siviloglou, G. A., and Christodoulides, D. N., "Curved plasma channel generation using ultraintense Airy beams," *Science* **324**(5924), 229–232 (2009).

[10] Polynkin, P., Kolesik, M., Roberts, A., Faccio, D., Trapani, P. D., and Moloney, J., "Generation of extended plasma channels in air using femtosecond Bessel beams," *Opt. Express* **16**, 15733–15740 (2008).

[11] Polesana, P., Franco, M., Couairon, A., Faccio, D., and Di Trapani, P., "Filamentation in Kerr media from pulsed Bessel beams," *Phys. Rev. A* **77**, 043814 (2008).

[12] Ament, C., Polynkin, P., and Moloney, J. V., "Supercontinuum generation with femtosecond self-healing Airy pulses," *Phys. Rev. Lett.* **107**, 243901 (2011).

[13] Chong, A., Renninger, W. H., Christodoulides, D. N., and Wise, F. W., "Airy-Bessel wave packets as versatile linear light bullets," *Nat. Photonics* **4**, 103–106 (2010).

[14] Bhuyan, M. K., Velpula, P. K., Colombier, J. P., Olivier, T., Faure, N., and Stoian, R., "Single-shot high aspect ratio bulk nanostructuring of fused silica using chirp-controlled ultrafast laser Bessel beams," *Appl. Phys. Lett.* **104**(2), – (2014).

[15] Amako, J., Sawaki, D., and Fujii, E., "Microstructuring transparent materials by use of nondiffracting ultrashort pulse beams generated by diffractive optics," *J. Opt. Soc. Am. B* **20**, 2562–2568 (2003).

[16] Bhuyan, M. K., Courvoisier, F., Lacourt, P.-A., Jacquot, M., Furfaro, L., Withford, M. J., and Dudley, J. M., "High aspect ratio taper-free microchannel fabrication using femtosecond Bessel beams," *Opt. Express* **18**, 566–574 (2010).

[17] Zhu, G., van Howe, J., Durst, M., Zipfel, W., and Xu, C., "Simultaneous spatial and temporal focusing of femtosecond pulses," *Opt. Express* **13**, 2153–2159 (2005).

[18] Oron, D. and Silberberg, Y., "Spatiotemporal coherent control using shaped, temporally focused pulses," *Opt. Express* **13**, 9903–9908 (2005).

[19] Clerici, M., Faccio, D., Rubino, E., Lotti, A., Couairon, A., and Trapani, P. D., "Space-time focusing of Bessel-like pulses," *Opt. Lett.* **35**, 3267–3269 (2010).

[20] He, F., Xu, H., Cheng, Y., Ni, J., Xiong, H., Xu, Z., Sugioka, K., and Midorikawa, K., "Fabrication of microfluidic channels with a circular cross section using spatiotemporally focused femtosecond laser pulses," *Opt. Lett.* **35**, 1106–1108 (2010).

[21] Zeng, B., Chu, W., Gao, H., Liu, W., Li, G., Zhang, H., Yao, J., Ni, J., Chin, S. L., Cheng, Y., and Xu, Z., "Enhancement of peak intensity in a filament core with spatiotemporally focused femtosecond laser pulses," *Phys. Rev. A* **84**, 063819 (2011).

[22] Kammel, R., Ackermann, R., Thomas, J., Götte, J., Skupin, S., Tünnermann, A., and Nolte, S., "Enhancing precision in fs-laser material processing by simultaneous spatial and temporal focusing," *Light Sci. Appl.* **3**, e169 (2014).

[23] He, F., Zeng, B., Chu, W., Ni, J., Sugioka, K., Cheng, Y., and Durfee, C. G., "Characterization and control of peak intensity distribution at the focus of a spatiotemporally focused femtosecond laser beam," *Opt. Express* **22**, 9734–9748 (2014).

[24] Vitek, D. N., Adams, D. E., Johnson, A., Tsai, P. S., Backus, S., Durfee, C. G., Kleinfeld, D., and Squier, J. A., "Temporally focused femtosecond laser pulses for low numerical aperture micromachining through optically transparent materials," *Opt. Express* **18**, 18086–18094 (2010).

[25] Vitek, D. N., Block, E., Bellouard, Y., Adams, D. E., Backus, S., Kleinfeld, D., Durfee, C. G., and Squier, J. A., "Spatio-temporally focused femtosecond laser pulses for nonreciprocal writing in optically transparent materials," *Opt. Express* **18**, 24673–24678 (2010).

[26] Block, E., Greco, M., Vitek, D., Masihzadeh, O., Ammar, D. A., Kahook, M. Y., Mandava, N., Durfee, C., and Squier, J., "Simultaneous spatial and temporal focusing for tissue ablation," *Biomed. Opt. Express* **4**, 831–841 (2013).

[27] Kolesik, M., Moloney, J. V., and Mlejnek, M., "Unidirectional optical pulse propagation equation," *Phys. Rev. Lett.* **89**, 283902 (2002).

[28] Couairon, A., Brambilla, E., Corti, T., Majus, D., de J. Ramírez-Góngora, O., and Kolesik, M., "Practitioner's guide to laser pulse propagation models and simulation," *Eur. Phys. J. Spec. Top.* **199**(1), 5–76 (2011).

[29] Johnson, H., "An improved method for computing a discrete Hankel transform," *Computer Physics Communications* **43**(2), 181 – 202 (1987).

[30] Guizar-Sicairos, M. and Gutiérrez-Vega, J. C., "Computation of quasi-discrete Hankel transforms of integer order for propagating optical wave fields," *J. Opt. Soc. Am. A* **21**, 53–58 (2004).

[31] Baddour, N. and Chouinard, U., "Theory and operational rules for the discrete Hankel transform," *J. Opt. Soc. Am. A* **32**, 611–622 (2015).

[32] Keldysh, L. V., "Ionization in the field of a strong electromagnetic wave," *Sov. Phys. JETP* **20**(5), 1307 (1965).

[33] Diels, J.-C. and Rudolph, W., [*Ultrashort laser pulse phenomena*], Academic press, second ed. (2006).

[34] Baddour, N., "Application of the generalized shift operator to the Hankel transform," *SpringerPlus* **3**(1), 246 (2014).

[35] Levitan, B. M. and Litvinov, G. L., [*Generalized displacement operators*], Encyclopedia of Mathematics, Springer (2002).

[36] Martinez, O. E., "Grating and prism compressors in the case of finite beam size," *J. Opt. Soc. Am. B* **3**, 929–934 (1986).

[37] Baddour, N., "Operational and convolution properties of two-dimensional Fourier transforms in polar coordinates," *J. Opt. Soc. Am. A* **26**, 1767–1777 (2009).

[38] Porras, M. A., Borghi, R., and Santarsiero, M., "Suppression of dispersive broadening of light pulses with Bessel–Gauss beams," *Opt. Commun.* **206**(4–6), 235 – 241 (2002).

[39] Zamboni-Rached, M., Recami, E., and Hernández-Figueroa, H. E., [*Localized waves*], Ch. 2, John Wiley & Sons (2007).

[40] Kolesik, M., Wright, E. M., and Moloney, J. V., "Interpretation of the spectrally resolved far field of femtosecond pulses propagating in bulk nonlinear dispersive media," *Opt. Express* **13**, 10729–10741 (2005).

[41] Couairon, A. and Mysyrowicz, A., "Femtosecond filamentation in transparent media," *Physics Reports* **441**(2–4), 47 – 189 (2007).

[42] Winkler, S., Burakov, I., Stoian, R., Bulgakova, N., Husakou, A., Mermillod-Blondin, A., Rosenfeld, A., Ashkenasi, D., and Hertel, I., "Transient response of dielectric materials exposed to ultrafast laser radiation," *Appl. Phys. A* **84**(4), 413–422 (2006).